Beam image-shift accelerated data acquisition for near-atomic resolution single-particle cryo-electron tomography

Jonathan Bouvette[1#], Hsuan-Fu Liu [2#], Xiaochen Du[3,4], Ye Zhou[3], Andrew P. Sikkema[5], Juliana Da Fonseca Rezende E Mello[1], Bradley Klemm[1], Rick Huang[6], Roel M. Schaaper[1], Mario J. Borgnia[1*] and Alberto Bartesaghi[2,3,7*]

[1] Genome Integrity and Structural Biology Laboratory, National Institute of Environmental Health Sciences, National Institutes of Health, Department of Health and Human Services, Research Triangle Park, NC, 27709, USA

[2] Department of Biochemistry, Duke University, Durham, NC, 27708, USA

[3] Department of Computer Science, Duke University, Durham, NC, 27708, USA

[4] Department of Chemistry, Duke University, Durham, NC, 27708, USA

[5] Epigenetics & Stem Cell Biology Laboratory, National Institute of Environmental Health Sciences, National Institutes of Health, Department of Health and Human Services, Research Triangle Park, NC, 27709, USA

[6] Laboratory of Cell Biology, Center for Cancer Research, National Cancer Institute, National Institutes of Health, Department of Health and Human Services, Bethesda, MD, 20892, USA

[7] Department of Electrical and Computer Engineering, Duke University, Durham, NC, 27708, USA

[#] These authors contributed equally

[*] Co-corresponding authors: mario.borgnia2@nih.gov, alberto.bartesaghi@duke.edu

ABSTRACT

Tomographic reconstruction of cryopreserved specimens imaged in an electron microscope followed by extraction and averaging of sub-volumes has been successfully used to derive atomic models of macromolecules in their biological environment. Eliminating biochemical isolation steps required by other techniques, this method opens up the cell to in-situ structural studies. However, the need to compensate for errors in targeting introduced during mechanical navigation of the specimen significantly slows down tomographic data collection thus limiting its practical value. Here, we introduce protocols for tilt-series acquisition and processing that are simultaneously consistent with high-throughput and high-resolution imaging. We achieve this by using beam-image shift to multiply the number of areas imaged at each stage position, by integrating geometrical constraints during imaging to achieve high precision targeting, and by performing per-tilt astigmatic CTF estimation and data-driven exposure weighting to improve final map resolution. We validated our beam image-shift electron cryo-tomography (BISECT) approach by determining the structure of a low molecular weight target (~300kDa) at 3.6 Å resolution where density for individual side chains is clearly resolved.

INTRODUCTION

Three-dimensional cryo-electron microscopy (cryo-EM) is now routinely used to determine the structure of macromolecular complexes at near-atomic resolution. The method consists in reconstructing the electron scattering map of a macromolecule of interest from projection images of cryopreserved specimens recorded in a transmission electron microscope. Electron radiation sensitivity limits the dose that can be used and consequently the signal-to-noise ratio (SNR) of molecular images. Single particle analysis (SPA) overcomes this limitation by averaging thousands of low dose images of randomly oriented but otherwise identical macromolecules. Tens to hundreds of individual molecular projections are typically captured in a snapshot of a single field of view. The relative orientation of each individual particle projection can be determined provided that images are recorded over a uniform background and that the projections do not overlap. These requirements preclude the applicability of SPA to important questions in which the complex of interest cannot be isolated from its crowded and variable biological context. This limitation can be overcome using cryo-electron tomography (CET), where the electron scattering map or tomogram of an individual pleomorphic object is reconstructed from a series of images recorded while tilting the stage.

Multiple instances of the same biological entity can thus be identified within their native context, extracted from several tomograms and combined using sub-volume averaging (SVA) to obtain a high-resolution map [1]–[5]. The resolution of structures determined by SVA is generally lower than SPA, in part due to difficulties in estimating the contrast transfer function (CTF) accurately, the lack of effective strategies to compensate for radiation damage and the challenges of collecting large datasets due to the slow speed of data collection. The first sub-nanometer

resolution structures determined by CET were obtained using the Constrained Single Particle Tomography (CSPT) approach [6], where the idea of working directly with the raw 2D projections extracted from the tilt-series and performing an SPA-like reconstruction was initially introduced. While the raw projections still carry information from the surrounding environment, image alignment based on the features of the repetitive structure will cause the variable signal from the background to be averaged out during 3D reconstruction. This hybrid strategy provides a convenient framework to analyze low contrast tomographic projections and produce high-resolution 3D maps by combining established principles for SPA image alignment and reconstruction, with enforcement of the tilt-geometry constraints. The general principle behind CSPT has since been successfully adopted by several image processing packages for CET/SVA [7]–[11]. Despite these and other advances, however, fundamental technical barriers still exist that have limited the application of CET/SVA to either lower resolution studies or to the analysis of well-behaved samples. Examples include structures of envelope glycoproteins attached to the surface of virions like HIV-1 [12], [13] and SARS-CoV-2 [14], [15] at sub-nanometer resolution, as well as near-atomic resolution studies of large-molecular weight targets like ribosomes [10], [16], or samples that display favorable spatial arrangements such as those present in quasi-crystalline formations of HIV-1 Gag polyprotein [17], [18].

Protocols for data collection in cryo-EM consist of executing repetitive cycles of targeting and imaging. It follows that the rate of data collection is inversely proportional to the time it takes to position the beam on a target area and acquire an exposure. While the speed of image recording devices has improved significantly over the past decade and the trend is likely to continue, navigation between targets is still performed by mechanically displacing the specimen-holding stage using step motors. With few exceptions, the mechanical stages in most instruments have

extremely limited in-plane precision (less than 200 nm) and poor eucentricity (~2 um variation). While targeting errors and drift can be monitored and corrected using a tracking area, this strategy introduces additional steps that further reduce acquisition speed. In SPA, targeting errors in the plane are seldom critical because each area is imaged only once and errors in Z-height only result in small variations in defocus that are corrected during data processing. In CET, however, each target needs to be imaged from multiple angles while maintaining the object of interest within a narrow field of view, and defocus is difficult to estimate because of the low SNR images. Thus, precise correction of spatial parameters becomes a time-consuming requirement that is critical for improving resolution. Recently, the use of fast detectors has allowed the collection of continuous tilt-series or fast incremental single exposure (FISE) in as little as 5 minutes [19], [20]. Part of the gain in speed is accomplished by skipping all real-time corrections while using a special high-eucentricity single-axis stage. Unfortunately, structures solved from data collected in this manner are poorly resolved compared to those resulting from more precisely corrected protocols for data collection.

When collecting data for SPA, navigating the local area electron-optically by using beam-tilt induced image-shift (BIS) is a fast and precise way to increase the number of targets acquired for each slow mechanical movement [19], [20]. Extending this approach to tomography seems counterintuitive as targeting errors in a tilted specimen are exacerbated, thus requiring increased tracking precision. Here, we show that achieving precise targeting when expanding the surveyed area by electronic navigation requires additional modeling of the specimen behavior. This strategy increases the number of targets collected per stage movement, thereby accelerating data collection without sacrificing resolution. Moreover, this method can be implemented on instruments without

specialized stages, and by virtue of limiting the number of mechanical movements required for navigation, it also reduces the wear on the stage.

To overcome the inherent low-throughput characteristic of CET data collection, improve the resolution of SVA and extend its application to a wider set of samples including low molecular weight targets, here, we: (1) use BIS navigation to multiply the number of regions of interest (ROI) imaged at each mechanical step, (2) integrate image processing into data collection to compensate the imprecision of the stage using geometrical constraints of multiplexed ROIs, and (3) introduce improved data processing routines for high-resolution structure determination using CET/SVA. Our beam image-shift electron cryo-tomography (BISECT) approach can produce tilt-series that simultaneously match the quality of data obtained by the dose-symmetric tilt-scheme [21], and the speed of FISE [22], effectively combining their benefits. During data processing, we improve map resolution by implementing accurate per-tilt astigmatic CTF estimation and self-tuning routines for exposure weighting during 3D reconstruction. To validate our approach, we collected tilt-series using BISECT and determined the 3.6 Å resolution structure of a low molecular weight target (~300kDa) using CSPT, indicating that complexes within this size range are now within the reach of this technique. The advances reported here considerably improve the technical capability of CET, bringing this technology a step closer to becoming a high-throughput tool for *in-situ* structure determination.

RESULTS

Electronic navigation for multiplexed collection of neighboring ROIs

Achieving sub-nanometer resolution in CET requires the combination of multiple tightly overlapping projections of each ROI recorded from different angles and with a well-defined defocus. Tracking areas are often used to estimate the deviations induced from mechanically tilting the sample and compensate them to ensure precise targeting. This time-consuming step can be turned into an advantage provided that the model used for compensating the errors is precise enough to enable targeting of adjacent ROIs by electronic means, thus dividing its cost by the number of multiplexed targets. To successfully implement this beam-image shift enhanced cryo-tomography, the movement of each ROI in all three dimensions needs to be considered. As the stage is tilted, targets that do not lie along the tilt axis will move away from the focus plane (Z-axis) and inwards towards the tilt axis, **Figure 1A**. Using the same tracking principle to re-center on the target area, we can estimate the new positions of each ROI from their previous location. Each ROI image contributes new tracking information to complete the model thus progressively improving it (**Supplementary Figure 1)**. Using this procedure, it is possible to set up image-shift patterns following a regular holey lattice or custom patterns where each ROI is manually chosen, **Figure 1B**.

To satisfy the sampling rate requirements of imaging at near-atomic resolution, pixel sizes of 1.5 Å or smaller need to be used. At these magnifications, the field of view is rather small on the detector (≤ 600 nm on a K2 summit) while the precision of the stage is in the same order of magnitude (200 nm for a Titan Krios). Without performing corrections between tilts, the targeted

area would drift outside the field of view, especially when using a dose-symmetric scheme in which the stage is subject to large rotations [23]. To solve this problem, we adopted a two-step targeting strategy consisting of a coarse correction at low magnification followed by a second more accurate tracking step at the target magnification. This allows the acquisition of tilt-series at small pixel sizes without the need of a highly eucentric holder. As any resulting error in tracking is translated to all ROIs, we realized that achieving the necessary precision on the image-shift areas required an accuracy of <10 nm of the tracking area. The current implementation of tracking in SerialEM [24] correlates the current tracking image with the previous one on the same branch (positive or negative) of the tilt-series. Unfortunately, cross correlation alignment of noisy images often leads to erroneous estimations of displacement. When shifts are calculated solely in relation to the last image from the same branch, tracking errors accumulate over the course of data collection leading to significant deviations from the target. To improve precision and robustness, we calculated the displacement relative to the whole tracking series by iteratively aligning the cosine stretched images. To verify the correctness of the alignment, a new image is recorded after the calculated shifts are applied and the alignment process is repeated until a pre-established threshold is reached. Combined with the two-step tracking procedure (with thresholds of 100 nm and 5 nm at the low and high magnification levels, respectively), this approach yields a tracking precision better than 10 nm over the entire course of the tilt-series, **Supplementary Movie 1**.

After implementing the tracking procedure described above and correcting for the image-shift of area locations using basic geometry relationships, we achieved a targeting precision that allowed successful tomogram reconstruction at high magnification. However, we observed that errors were inconsistent across different ROIs, resulting in many tilt-series moving off target. These errors in targeting also led to a wide spread of defocus across the tilt-series since the estimation of the

vertical displacement of each ROI was dependent on a precise in-plane targeting. We realized that the basic geometric model was valid only when ROIs are co-planar with the focus/tracking area and that variations in the topography of the grid as small as 100 nm can be highly detrimental to targeting, **Figure 2A**. By fitting axis rotation equations to the targeting data, we can get an initial estimation of the eucentric height for all ROIs using as few as the first five data points. From this fit, new image shift coordinates and defocus corrections are calculated using the more accurate geometric relationships and the fit is refined with each additional point (Online Methods). This strategy minimizes the targeting errors and the defocus variations over the tilt-series, **Figure 2B-C**. Generally, the targeting is within 0.067 ± 0.124 µm (median ± IQR) and the defocus is within 0.21 ± 0.17 µm over the course of a tilt-series across image-shift areas up to the tested 8 µm distance from the tracking area (124 μm^2 total area, 25 holes on R1.2/1.3 holey grids). Interestingly, targeting and defocus errors for each ROI bear no proportion to its BIS distance from the tracking area. In fact, we've observed that one of the most distal ROIs requiring a 7.2 µm BIS bore a near perfect targeting with a maximal in plane displacement of 68 nm and a variation in defocus of 0.48 µm across the entire tilt-series **Supplementary Movie 2**. These results show that implementation of BISECT is feasible and that the current precision we achieve during targeting should allow for the use of even larger acquisition areas.

Tilted-CTF determination from low-dose tomographic tilt-series

Accurate defocus estimation is critical for correctly performing deconvolution of the CTF during 3D reconstruction and a prerequisite for achieving high-resolution. Small errors arising from imprecisions in the detection of zero-crossings can lead to signal attenuation, particularly at the

high-resolution range. While strategies for fully astigmatic defocus estimation and correction are used routinely in SPA, their use in CET has been challenging for two main reasons: (1) the lower contrast of dose-fractionated tilted projections produces weak Thon rings that make defocus estimation unreliable, and (2) accounting for the defocus gradient induced by tilting requires the use of more sophisticated strategies for CTF estimation. To overcome these challenges, early attempts assumed eucentricity of the tilt-series and used iso-defocus strips running parallel to the tilt-axis to estimate defocus [25]. Other approaches estimate defocus for subsets of projections [26], assume negligible astigmatism [7], or impose a single astigmatism value per tilt-series [10]. Meanwhile, strategies for collecting projections of tilted specimens were introduced in SPA for addressing problems of preferred orientation [27]. This led to the development of programs for tilted defocus determination that can estimate the orientation of the tilt-axis and the tilt-angle based on local changes in estimated defocus [28]–[31]. While the lower doses used in tomography in principle prevent these strategies from working on tilt-series images, we reasoned that since the tilt-axis and tilt-angle for each projection is determined precisely during tilt-series alignment [32], these values could simply be used as input to one of the tilted CTF estimation routines used in SPA. This approach allowed us to reliably estimate defocus and astigmatism for each image in a tilt-series even at high-tilt angles, **Figure 3**.

Constrained projection refinement and self-tuning exposure weighting

As initially proposed in the CSPT approach [6], we carry out all 3D reconstruction and refinement operations using 2D particle projections extracted directly from the raw tilt-series. The rationale for this approach is based on the following principles: (1) it minimizes the number of intermediate image interpolation steps necessary to go from raw 2D data to 3D reconstruction thus lowering

computational b-factors, (2) modeling each sub-volume as a set of 2D projections related by the parameters of the tilt-geometry eliminates the need to deal with the missing-wedge avoiding its detrimental effects on image alignment and reconstruction, and (3) imposing geometric tomographic constraints during refinement improves image alignment accuracy. In addition to these features, we improved the original CSPT algorithm by using newer components for 3D alignment and reconstruction to benefit from the latest algorithmic advances in SPA, and implemented more accurate strategies for assigning per-particle CTF parameters based on the new astigmatic tilted-CTF model and the position of particles within tomograms, **Supplementary Figure 2**. In order to maximize the recovery of high-resolution information during 3D reconstruction and compensate for the effects of radiation damage and increased sample thickness due to tilting, we also implemented a new data-driven exposure weighting routine similar to the one we used to improve SPA reconstructions [33]. Unlike weighting strategies used for movie frames, tilted particle projections are not all in the same plane requiring implementation of the exposure filter in three dimensions (as part of the reconstruction routine). We start by measuring the relative quality of each projection through evaluation of the similarity of each image with respect to the corresponding slice from the most recent 3D reconstruction. To overcome the problems associated with measuring similarity scores from noisy individual particle projections and prevent overfitting, the exposure weights are estimated based on the average similarity across all particle projections in each tilt-angle, **Figure 4A**. The newly derived weights automatically reduce the contribution of high-tilt images or projections taken later in the tilt-series, allowing us to more efficiently extract high-resolution information from the raw tilt-series data, **Figure 4B**. Since our strategy is purely data-driven, it requires no knowledge of the tilting scheme used during data collection and/or the electron exposure used for imaging which can be difficult to determine

accurately in practice. With these improvements, the new algorithm achieves higher resolution, reduces overfitting and as a result can be applied to a broader range of samples including low-molecular weight targets.

3.6 Å resolution structure of 300kDa complex using BISECT/CSPT

We imaged a monodisperse sample of protein VC1979 of *Vibrio cholerae* (dNTPase), an HD-domain family protein and a homolog of SAMHD1 and E. coli dGTP triphosphohydrolase. dNTPase is a homohexamer with D3 symmetry and a total molecular weight of ~300kDa. We collected 11 areas of 25 holes for a total of 275 tilt-series using a K2 camera (~5 min per tilt-series). The on-the-fly cross-correlation tracking of the areas was within 220 nm for each position and the defocus estimation of individual images was within 0.4 µm, **Figure 2C**. We estimated the tilted CTF for each projection independently and selected 64 tilt-series based on the absence of ice contaminants and the best estimated CTF resolution, **Supplementary Figure 3**. From the reconstructed tomograms, 34,435 particles were extracted and subjected to sub-volume averaging followed by CSPT refinement, resulting in a 3.6 Å resolution map where density for side chains could be clearly visualized, **Figure 5**. This result validates the effectiveness of our combined approach for high-speed data collection and high-resolution CET/SVA data processing. We also compared the quality of our BISECT/CSPT structure against standard SPA reconstruction using images acquired from the same grid. We collected a single-particle dataset consisting of 2,275 movies (using the same 25 holes BIS scheme) and extracted a similar number of particles as in the CSPT reconstruction (~34k) from the best 64 micrographs, yielding a reconstruction at 3.3 Å resolution using existing protocols for SPA refinement [33], **Figure 6A**. The improvement in resolution is consistent with the higher quality of the SPA images resulting from choosing only

the top 3% of movies (64 out of 2,275) to produce the final map (vs. 64 out of 275 tilt-series used in the CSPT reconstruction). In addition, the cumulative effects of beam-induced motion are likely more pronounced in tomography due to the use of multiple shorter exposures (as opposed to a single long exposure in SPA), also contributing to the lower resolution. Despite the reduced overall quality of the CSPT reconstruction, both maps show similar density for individual side chains in the ordered regions, **Figure 6** and **Supplementary Figure 4**, suggesting that under otherwise equal experimental conditions, BISECT combined with CSPT can produce near-atomic resolution maps of comparable quality to SPA.

DISCUSSION

While the number of SPA structures deposited in the Electron Microscopy Data Bank (EMDB) continues to increase, progress in CET has been slower due in part to the technical challenges involved in imaging crowded specimens using low-dose settings. Here, we present a platform for tilt-series data collection and processing that significantly improves the technical capability of CET, paving the way for the routine visualization of targets in-situ at near-atomic resolution. By simultaneously achieving high-quality and high-speed data acquisition in combination with effective strategies for data processing, our methods can streamline the determination of high-resolution structures and provide a path for imaging targets present at low concentrations within their native environments which are not tractable by current low-throughput methods.

Our approach extends the single tilt BIS strategy widely used in SPA to the case of tilted data collection for tomography. This is accomplished by modeling the behavior of the specimen in real

time to increase the accuracy of electronic navigation to multiple areas. The resulting flexible framework can also be used to implement hybrid strategies for data collection, for example, by allowing the acquisition of fewer and more widely spaced tilts. Fractionating the dose into fewer exposures could result in more accurate CTF determination and improved image alignment, potentially leading to higher resolutions. In the current implementation, we use a separate computer to calculate the corrections in real time. The results are then transmitted to the data collection software to maintain the target within the field of view of the detector. This configuration is adaptable to existing imaging setups with virtually no modification. A powerful alternative would be to perform these calculations directly at the processing unit of the detector and send the appropriate corrections to the microscope computer. This would allow the detector to lock onto the field of view for each ROI. The resulting improvement in speed may make it possible to combine BIS multiplexed data collection with FISE without sacrificing resolution.

Our strategy for data processing capitalizes on recent advances in SPA by repurposing these tools to work on low-dose projections extracted from tomographic tilt-series. Imposition of the constraints of the tilt-geometry during refinement and reconstruction allows us to accurately align particle projections and correct for the CTF while minimizing overfitting. While we currently cannot assess the effects of beam-tilt in the resolution of the dNTPase structure (due to the low contrast in the images), we expect these effects to be similar in magnitude to those observed in SPA [19], [34]. In the future, extension of beam-tilt correction strategies currently used in SPA [35], [36] to CET could result in further improvements in map quality. This and future developments in data processing will result in additional improvements in resolution that could soon allow application of these methods to even lower molecular weight targets (<300kDa).

According to the EMDB, there are 13 structures determined by CET/SVA at resolutions better than 4.5Å and the number of particles required to reach those resolutions is on average ~90,000 sub-volumes. Since the map we obtained for dNTPase used only ~30k particles, our results indicate that achieving near-atomic resolution using BISECT combined with CSPT may require significantly smaller datasets than previously anticipated. The lower particle requirements combined with the faster speed of acquisition, may have implications for the feasibility of cellular CET/SVA studies of rare molecular species that may be present at low concentrations under physiological conditions.

While SPA has been the flagship modality of cryo-EM to determine structures of proteins in monodisperse state at ever increasing resolutions, the advent of technological advances in CET like the ones reported here will pave the way for this technique to become an effective strategy for routinely studying protein complexes at near-atomic resolution within the functional context of the cell. Importantly, at these resolutions, the visualization of individual side chains greatly facilitates the placement of atomic models into the cryo-EM maps, resulting in more accurate structures. Ultimately, these methods will help close the resolution gap between high-resolution strategies used to study molecular assemblies reconstituted in-vitro like X-ray crystallography and single-particle cryo-EM, and techniques for in-situ structure determination like CET.

ONLINE METHODS

Sample preparation

dNTPase was expressed from the pMCSG7-dNTPase vector in BL21(DE3) and grown in Terrific Broth (TB) medium with 4% glycerol and ampicillin (100 µg/mg) induced with IPTG (final concentration 0.2 mM), and grown for an additional 14-18 hrs at 20°C before harvesting by centrifugation. Cell pellets were resuspended in approximately 5 mL Buffer A (100 mM Tris pH 7.9, 500 mM NaCl, 30mM imidazole, 5% glycerol) per 1 g of cell paste. All purification steps were performed at 4°C. Resuspended cells were incubated with DNase (4 mg), lysozyme (40 mg), and $MgCl_2$ (2mM). Cells were lysed by three 1 min sonication cycles at 60% power using a Branson 450 Digital Sonifier with at least 2 minutes between cycles and clarified by centrifugation at 30,0000 x g for 30 minutes. The soluble fractions were loaded onto a 5-mL HisTrap Ni-NTA column (GE Healthcare) in Buffer A and eluted with an imidazole gradient from 60 to 300mM. Sample was dialyzed overnight into Buffer B (50 mM Tris pH 7.9, 100 mM NaCl, 5% glycerol) at 4°C and treated with tobacco etch virus (TEV) protease (1:30 ratio TEV:dNTPase plus 2 mM DTT) to remove the purification (polyhistidine) tag, and then applied to a 5-mL HisTrap Ni NTA column. The flow-through fraction was further purified by size exclusion chromatography with a HiLoad 16/600 Superdex 200 column (GE Healthcare) in Buffer C (50 mM Tris pH 7.9, 100 mM NaCl, 10% glycerol). Peak fractions were pooled, concentrated to 10-20mg/mL, aliquoted, flash cooled with liquid N_2, and stored at -80°C.

Grid preparation

1-1.5mg protein was thawed then run over a 10/30 Superdex 200 Increase column (GE Healthcare) in Buffer E (20mM Tris pH 7.5, 100mM NaCl). 2 parts of the peak fraction at about 1.3 mg/mL

was mixed of with 1 part of 6 nm gold fiducials that were 20x concentrated and buffer exchanged in Buffer E. 3uL of the mix was applied on a UltrAuFoil R1.2/1.3 300 mesh grid (Quantifoil Micro Tools GmbH). Grids were previously glow-discharged for 30 sec at 15 mA (PELCO easiGlow™, Ted Pella, Inc.). Excess sample was removed by blotting for 3 s using filter paper (Whatman #1) and grids were plunged-frozen in liquid ethane (-182 °C) using a vitrification robot (EM GP2, Leica Microsystems).

Data collection

Data were collected at 300 keV under parallel beam illumination on a Titan Krios (Thermo Fisher Scientific) housed at the NCI cryoEM facility affiliated with the NIH IRP CryoEM Consortium (NICE). Images were recorded on a direct electron detector (K2 summit, Gatan Inc.) placed behind an energy filter (Bioquantum, Gatan Inc.) operated with a 20 eV slit. Tilt-series were collected using SerialEM (version 3.8beta8) [24]. An initial set of 125 tilt-series were collected using a ±60° range grouped dose-symmetric scheme (0, 3, -3, -6, 6, 9, -9, -12, 12, 15, -15, -18, -21, 18, 21, 24, 27, -24, -27, -30, -33, 30, 33, 36, 39, 42, -36, -39, -42, -45, -48, 45, 48, 51, 54, 57, 60, -51, -54, -57, -60) with a dose of ~ 3e^-/Å^2 per tilt angle (4 frames per movie, ~120 e^-/Å^2 total dose). An additional 275 tilt-series were collected using a similar tilt scheme as before but with a ± 36° range (0, 3, -3, -6, 6, 9, -9, -12, 12, 15, -15, -18, -21, 18, 21, 24, -24, -27, -30, 27, 30, 33, 36, -33, -36) and a dose of ~5e^-/Å^2 per tilt angle (11 frames per movie, ~120 e^-/Å^2 total dose). The SPA dataset was collected using a total dose of ~60 e^-/Å^2. For all 3 datasets, each area was collected with a pixel size of 1.37 Å/pix using a 5x5-hole lattice with the stage centered on the target area and each hole acquired using BIS. The initial set of tilt-series was used exclusively to evaluate our data

acquisition protocols, while the other two datasets were used for structure determination by CSPT and SPA, respectively.

BISECT protocol for tilt-series data collection

A set of routines written in Python were used externally to track the tilt-series and correct for the image-shift coordinates and defocus positions. Tracking was done in 2 steps: (1) a low-magnification tracking step at 5.2 Å/pix with a threshold 100 nm, and (2) a high-magnification tracking step with a threshold of 5 nm. tiltxcorr [24], [32] was used to calculate the global displacement of each tilt with respect to the initial image. Tracking was corrected with image shift and iterated until the thresholds above were met. Targeting corrections for the ROIs also used tiltxcorr to calculate the alignments. The Z-height estimation was done with the fitting cartesian rotation of axis formula (Eq.1) to the y-coordinate of the target. After fitting for z, the new values of y and defocus (z) were calculated using Eq. 1 and Eq. 2.:

$$y' = y\ \cos\theta + z\sin\theta \qquad \text{Eq. 1}$$
$$z' = -\ y\ \sin\theta + z\cos\theta \qquad \text{Eq. 2}$$

where, θ is the tilt angle in degrees. CTF estimation of each individual image during acquisition was estimated with CTFFIND4 [37].

Data collection times

The speed of data collection varied with the type of microscope and detector used. Benchmarks were done using a 25-hole (5 x 5 lattice) BIS pattern, and a dose-symmetric scheme running at ± 60° with 3° increments and 3 $e^-/Å^2$/tilt. On a Talos Arctica equipped with a K2 detector, we could achieve 8.1 min per tilt-series. Similarly, on a Titan Krios equipped with a K2 detector we achieved 7.9 min per tilt-series. Finally, on a Titan Krios equipped with a K3 detector, we could achieve 3.1

min per tilt-series. The rate limiting step is the tracking routine, since the microscope has to wait for the alignments to return before starting the next step, while the alignment of the image-shift areas can occur before the start of the next cycle. The speeds achieved by BISECT are similar to those achieved by the FISE data collection scheme [22], [38].

Determination of tilted-CTF model from tomographic tilt-series

In order to estimate the defocus gradient of individual tilted projections, we first performed tilt-series alignment using routines implemented in the program IMOD [32]. The orientation of the tilt-axis and the tilt-angle for each projection were used as input to an updated version of the program CTFFIND4 [37] that is part of the latest development version of cisTEM [35], available at https://github.com/ngrigorieff/cisTEM. It includes a new feature to determine the tilt angle and tilt axis in images of tilted specimens. The original code was adapted by simply disabling the search for the tilt-angle and tilt-axis orientation, and instead using the values determined during tilt-series alignment to calculate a single corrected power spectrum. Using this approach, we could accurately estimate the three CTF parameters for each projection in the tilt-series, **Figure 3**.

3D refinement and data-driven exposure weighting

After tomogram reconstruction, a low-resolution initial model was obtained using sub-volume averaging, and particle projections from all sub-volumes were subsequently extracted and merged into one large particle stack while keeping track of the particle identities, parameters of the tilt-geometry and the per-particle defocus, **Supplementary Figure 2**. Sub-volume orientations and the parameters of the tilt-geometry parameters were then refined using CSPT. Similarity scores were assigned to individual particle projections using the refine3d routine implemented in the

cisTEM package [35]. To obtain the new exposure filter, score averages over all particles in a tilt-series were calculated and used inside a modified version of cisTEM's reconstruct3d program to implement the weighting. As expected, the measured score averages successfully captured the relative differences in image quality characteristic of the dose-symmetric tilt-scheme and the predicted effects of radiation damage, **Figure 4A**. The corresponding 2D frequency weights were derived using the same formula we implemented for exposure filtering in SPA [33], **Figure 4B**.

Near-atomic resolution structure of dNTPase

The set of 275 raw tilt-series was first subjected to the standard CET processing pipeline including tilt-series alignment and reconstruction as implemented in the package IMOD [32]. Astigmatic tilted-CTF models were determined for each tilted projection and the 64 tilt-series containing the highest resolution signal were selected for further processing. 34,435 particles were manually selected from the tomographic reconstructions and subjected to sub-volume averaging and classification as implemented in the EMAN2 package [7], resulting in a 6.4 Å resolution reconstruction. Particle projections were then extracted from the raw tilt-series and defocus values assigned based on the position of each particle within the tomogram. Particle projections were then merged in 3D using standard SPA routines implemented in cisTEM [35], followed by constrained refinement of particle orientations and parameters of the tilt-geometry using CSPT [6]. Final map resolution was estimated using the Fourier Shell Correlation criteria (0.143-cutoff) between half maps. For post-processing, maps were sharpened with phenix.resolve_cryo_em using as inputs the unfiltered half maps, the molecular weight of the complex, and a soft shape mask [39]. An atomic model from X-ray crystallography was fit into the cryo-EM maps for visualization. Additional data processing statistics are included in **Supplementary Table 1**.

ACCESSION CODES

Cryo-EM density maps of dNTPase determined using BISECT/CSPT and regular SPA have been deposited with the Electron Microscopy Data Bank (EMDB) with accession codes EMDxxxxx and EMDxxxxx, respectively. The atomic model of dNTPase is available from the Protein Data Bank (PDB) with accession code XXXX.

CODE AVAILABILITY

The SerialEM and Python scripts used to implement BISECT, and the code for CTF estimation and CSTP refinement and reconstruction will be made available through the SerialEM Script Repository (https://serialemscripts.nexperion.net/) and Gitlab, respectively.

ACKNOWLEDGMENTS

We thank Qinwen Huang for assistance with data processing and James Horng for his role in the protein expression and purification. This work was supported in part by the Intramural Research Program of the NIH; National Institute of Environmental Health Sciences (ZIC ES103326 to M.J.B.). This study utilized the computational resources offered by Duke Research Computing (http://rc.duke.edu). We thank Tim Grant and Niko Grigorieff for making the development version of CTFFIND4 available to us. We thank Mark DeLong, Charley Kneifel, Mike Newton, Victor Orlikowski, Tom Milledge, and David Lane from the Duke Office of Information Technology and Research Computing for providing assistance with the computing environment.

AUTHOR CONTRIBUTIONS

J.B. and M.J.B. developed and implemented BISECT, H.L., X.D. and A.B. developed and implemented CSPT, A.P.S., B.K. and R.M.S. developed the V. cholerae VC1979 project, including the cloning and purification of the protein, J.B. and J.F.R.M. prepared specimens, J.B. and R.H. collected data, J.B., H.L.,Y.Z., and A.B. did the data analysis, J.B., H.L., M.J.B and A.B. wrote the paper, J.B., H.L., Y.Z. and A.B. prepared the figures, and M.J.B. and A.B. conceived the project.

COMPETING FINANCIAL INTERESTS

The authors declare no competing financial interests.

REFERENCES

[1] A. Bartesaghi, P. Sprechmann, J. Liu, G. Randall, G. Sapiro, and S. Subramaniam, "Classification and 3D averaging with missing wedge correction in biological electron tomography☆," *J. Struct. Biol.*, vol. 162, no. 3, pp. 436–450, 2008, doi: 10.1016/j.jsb.2008.02.008.

[2] H. Winkler, P. Zhu, J. Liu, F. Ye, K. H. Roux, and K. A. Taylor, "Tomographic subvolume alignment and subvolume classification applied to myosin V and SIV envelope spikes.," *J. Struct. Biol.*, vol. 165, no. 2, pp. 64–77, 2009, doi: 10.1016/j.jsb.2008.10.004.

[3] F. Förster, S. Pruggnaller, A. Seybert, and A. S. Frangakis, "Classification of cryo-electron sub-tomograms using constrained correlation.," *J. Struct. Biol.*, vol. 161, no. 3, pp. 276–86, 2008, doi: 10.1016/j.jsb.2007.07.006.

[4] D. Castaño-Díez, M. Kudryashev, M. Arheit, and H. Stahlberg, "Dynamo: a flexible, user-friendly development tool for subtomogram averaging of cryo-EM data in high-performance computing environments.," *J. Struct. Biol.*, vol. 178, no. 2, pp. 139–51, 2012, doi: 10.1016/j.jsb.2011.12.017.

[5] T. A. M. Bharat and S. H. W. Scheres, "Resolving macromolecular structures from electron cryo-tomography data using subtomogram averaging in RELION," *Nat. Protoc.*, vol. 11, no. 11, pp. 2054–2065, 2016, doi: 10.1038/nprot.2016.124.

[6] A. Bartesaghi, F. Lecumberry, G. Sapiro, and S. Subramaniam, "Protein secondary structure determination by constrained single-particle cryo-electron tomography," *Structure*, vol. 20, no. 12, pp. 2003–2013, 2012, doi: 10.1016/j.str.2012.10.016.

[7] M. Chen, J. M. Bell, X. Shi, S. Y. Sun, Z. Wang, and S. J. Ludtke, "A complete data processing workflow for cryo-ET and subtomogram averaging," *Nat. Methods*, vol. 16,

no. 11, pp. 1161–1168, Nov. 2019, doi: 10.1038/s41592-019-0591-8.

[8] B. A. Himes and P. Zhang, "emClarity: software for high-resolution cryo-electron tomography and subtomogram averaging," *Nat. Methods*, vol. 15, no. 11, pp. 955–961, 2018, doi: 10.1038/s41592-018-0167-z.

[9] K. Song, Z. Shang, X. Fu, X. Lou, N. Grigorieff, and D. Nicastro, "In situ structure determination at nanometer resolution using TYGRESS," *Nat. Methods*, vol. 17, no. 2, pp. 201–208, Feb. 2020, doi: 10.1038/s41592-019-0651-0.

[10] D. Tegunov, L. Xue, C. Dienemann, P. Cramer, and J. Mahamid, "Multi-particle cryo-EM refinement with M visualizes ribosome-antibiotic complex at 3.7 Å inside cells," *bioRxiv*, p. 2020.06.05.136341, Jun. 2020, doi: 10.1101/2020.06.05.136341.

[11] R. M. Sanchez, Y. Zhang, W. Chen, L. Dietrich, and M. Kudryashev, "Subnanometer-resolution structure determination in situ by hybrid subtomogram averaging - single particle cryo-EM," *Nat. Commun.*, vol. 11, no. 1, p. 3709, Dec. 2020, doi: 10.1038/s41467-020-17466-0.

[12] J. Liu, A. Bartesaghi, M. J. Borgnia, G. Sapiro, and S. Subramaniam, "Molecular architecture of native HIV-1 gp120 trimers," *Nature*, vol. 455, no. 7209, pp. 109–113, 2008, doi: 10.1038/nature07159.

[13] Z. Li *et al.*, "Subnanometer structures of HIV-1 envelope trimers on aldrithiol-2-inactivated virus particles," *Nat. Struct. Mol. Biol.*, pp. 1–9, Jun. 2020, doi: 10.1038/s41594-020-0452-2.

[14] B. Turoňová *et al.*, "In situ structural analysis of SARS-CoV-2 spike reveals flexibility mediated by three hinges," *Science (80-.).*, p. eabd5223, Aug. 2020, doi: 10.1126/science.abd5223.

[15] Z. Ke *et al.*, “Structures and distributions of SARS-CoV-2 spike proteins on intact virions,” *Nature*, pp. 1–7, Aug. 2020, doi: 10.1038/s41586-020-2665-2.

[16] R. Englmeier, S. Pfeffer, and F. Förster, “Structure of the Human Mitochondrial Ribosome Studied In Situ by Cryoelectron Tomography.,” *Structure*, vol. 25, no. 10, pp. 1574-1581.e2, 2017, doi: 10.1016/j.str.2017.07.011.

[17] F. K. M. Schur *et al.*, “An atomic model of HIV-1 capsid-SP1 reveals structures regulating assembly and maturation,” *Science (80-.).*, vol. 353, no. 6298, pp. 506–508, 2016, doi: 10.1126/science.aaf9620.

[18] S. Mattei, A. Tan, B. Glass, B. Müller, H.-G. Kräusslich, and J. A. G. Briggs, “High-resolution structures of HIV-1 Gag cleavage mutants determine structural switch for virus maturation.,” *Proc. Natl. Acad. Sci. U. S. A.*, vol. 115, no. 40, pp. E9401–E9410, Oct. 2018, doi: 10.1073/pnas.1811237115.

[19] A. Cheng *et al.*, “High resolution single particle cryo-electron microscopy using beam-image shift.,” *J. Struct. Biol.*, vol. 204, no. 2, pp. 270–275, 2018, doi: 10.1016/j.jsb.2018.07.015.

[20] C. Wu, X. Huang, J. Cheng, D. Zhu, and X. Zhang, “High-quality, high-throughput cryo-electron microscopy data collection via beam tilt and astigmatism-free beam-image shift,” *J. Struct. Biol.*, vol. 208, no. 3, p. 107396, Dec. 2019, doi: 10.1016/J.JSB.2019.09.013.

[21] W. J. H. Hagen, W. Wan, and J. A. G. Briggs, “Implementation of a cryo-electron tomography tilt-scheme optimized for high resolution subtomogram averaging,” *J. Struct. Biol.*, vol. 197, no. 2, pp. 191–198, 2017, doi: 10.1016/j.jsb.2016.06.007.

[22] G. Chreifi, S. Chen, L. A. Metskas, M. Kaplan, and G. J. Jensen, “Rapid tilt-series acquisition for electron cryotomography,” *J. Struct. Biol.*, vol. 205, no. 2, pp. 163–169,

Feb. 2019, doi: 10.1016/J.JSB.2018.12.008.

[23] W. J. H. Hagen, W. Wan, and J. A. G. Briggs, "Implementation of a cryo-electron tomography tilt-scheme optimized for high resolution subtomogram averaging," *J. Struct. Biol.*, vol. 197, no. 2, pp. 191–198, Feb. 2017, doi: 10.1016/J.JSB.2016.06.007.

[24] D. N. Mastronarde, "Automated electron microscope tomography using robust prediction of specimen movements," *J. Struct. Biol.*, vol. 152, no. 1, pp. 36–51, 2005, doi: 10.1016/j.jsb.2005.07.007.

[25] J. J. Fernández, S. Li, and R. A. Crowther, "CTF determination and correction in electron cryotomography.," *Ultramicroscopy*, vol. 106, no. 7, pp. 587–596, 2006.

[26] Q. Xiong, M. K. Morphew, C. L. Schwartz, A. H. Hoenger, and D. N. Mastronarde, "CTF determination and correction for low dose tomographic tilt series.," *J. Struct. Biol.*, vol. 168, no. 3, pp. 378–387, 2009.

[27] Y. Z. Tan *et al.*, "Addressing preferred specimen orientation in single-particle cryo-EM through tilting," *Nat. Methods*, vol. 14, no. 8, pp. 793–796, Aug. 2017, doi: 10.1038/nmeth.4347.

[28] J. A. Mindell and N. Grigorieff, "Accurate determination of local defocus and specimen tilt in electron microscopy.," *J. Struct. Biol.*, vol. 142, no. 3, pp. 334–47, 2003.

[29] M. Su, "goCTF: Geometrically optimized CTF determination for single-particle cryo-EM," *J. Struct. Biol.*, vol. 205, no. 1, pp. 22–29, Jan. 2019, doi: 10.1016/J.JSB.2018.11.012.

[30] K. Zhang, "Gctf: Real-time CTF determination and correction," *J. Struct. Biol.*, vol. 193, no. 1, pp. 1–12, 2016, doi: 10.1016/j.jsb.2015.11.003.

[31] D. Tegunov and P. Cramer, "Real-time cryo-electron microscopy data preprocessing with

Warp," *Nat. Methods*, vol. 16, no. 11, pp. 1146–1152, Nov. 2019, doi: 10.1038/s41592-019-0580-y.

[32] D. N. Mastronarde and S. R. Held, "Automated tilt series alignment and tomographic reconstruction in IMOD," *J. Struct. Biol.*, vol. 197, no. 2, pp. 102–113, 2017, doi: 10.1016/J.JSB.2016.07.011.

[33] A. Bartesaghi *et al.*, "Atomic Resolution Cryo-EM Structure of β-Galactosidase," *Structure*, vol. 26, no. 6, pp. 848-856.e3, 2018, doi: 10.1016/j.str.2018.04.004.

[34] C. Wu, X. Huang, J. Cheng, D. Zhu, and X. Zhang, "High-quality, high-throughput cryo-electron microscopy data collection via beam tilt and astigmatism-free beam-image shift," *J. Struct. Biol.*, vol. 208, no. 3, p. 107396, Dec. 2019, doi: 10.1016/J.JSB.2019.09.013.

[35] T. Grant, A. Rohou, and N. Grigorieff, "cisTEM, user-friendly software for single-particle image processing," *Elife*, vol. 7, no. e35383, 2018, doi: 10.7554/eLife.35383.

[36] J. Zivanov *et al.*, "New tools for automated high-resolution cryo-EM structure determination in RELION-3," *Elife*, vol. 7, no. e42166, 2018, doi: 10.7554/eLife.42166.

[37] A. Rohou and N. Grigorieff, "CTFFIND4: Fast and accurate defocus estimation from electron micrographs," *J. Struct. Biol.*, vol. 192, no. 2, pp. 216–221, Nov. 2015, doi: 10.1016/j.jsb.2015.08.008.

[38] F. Eisenstein, R. Danev, and M. Pilhofer, "Improved applicability and robustness of fast cryo-electron tomography data acquisition," *J. Struct. Biol.*, vol. 208, no. 2, pp. 107–114, Nov. 2019, doi: 10.1016/J.JSB.2019.08.006.

[39] T. C. Terwilliger, S. J. Ludtke, R. J. Read, P. D. Adams, and P. V. Afonine, "Improvement of cryo-EM maps by density modification," *Nat. Methods*, vol. 17, no. 9, pp. 923–927, Aug. 2020, doi: 10.1038/s41592-020-0914-9.

FIGURE LEGENDS

Figure 1: Parallel acquisition of tilt-series using beam-image shift electron cryo-tomography (BISECT). **(A)** Schematic of the movement of ROIs (white circles) from the initial position (gray) and after stage tilting (blue). **(B)** Evolution of the targeting and defocus over a 5x5-hole area. The initial field of view of each area is shown as red squares. The high-magnification tracking area is shown as an orange square. Lines show the movement of the targeting obtained from cross-correlation alignment (scaled by 5 for visualization) and are color coded according to the estimated defocus for each image.

Figure 2: Effects of eucentric plane correction during tilt-series acquisition. **(A-B)** Comparison of the target displacement during tilting assuming that the sample is flat (**A**, green arc) or when considering an off-plane shift (**B**, red arc). **(C)** Measurement of the median and inter quartile range (IQR) of displacement in the x-coordinate (red) and y-coordinate (blue) without correcting for off-plane shift (left panel) and with correction (right-panel) over multiple tilt-series (n=150). **(D)** Measurement of the median and IQR of the defocus variation from the first image without correcting for off-plane shift (left panel) or with correction (right-panel) over multiple tilt-series (n=150).

Figure 3: Astigmatic tilted-CTF determination from low-dose tomographic tilt-series. **(A)** 2D power spectra, fitted CTF model and corresponding 1D radial profile (red), estimated defocus (green dashed line), and CTFfit scores (blue) for projections at -51, 0 and 51°, respectively, from a tilt-series downloaded from EMPIAR-10453. **(B)** Astigmatic CTF estimation in the positive

branch of a tilt-series from the dNTPase sample using a +/-36º range. Plots show variations in the astigmatism angle (green) and defocus differences (blue) across the tilt range (top). Corresponding 2D power spectra obtained from tilt angles 0, 21 and 36° showing changes in astigmatism (bottom).

Figure 4: Self-tuning exposure weighting based on assigned particle scores. **(A)** Average similarity scores calculated over individual particle projections and plotted as a function of the tilt-angle revealing the expected characteristic of the dose-symmetric scheme showing higher quality data obtained at the lower tilts. **(B)** 2D plot showing the cumulative contribution of individual tilts to the 3D reconstruction as a function of spatial frequency. Each colored band represents one tilt. The high frequency information is contributed mostly by lower tilts which are also exposed first.

Figure 5: Near-atomic resolution structure of 300kDa complex using BISECT/CSPT. **(A)** 50nm-thick slice through tomographic reconstruction showing individual dNTPase particles. Scale bar 100nm. **(B)** Overview of dNTPase map obtained from ~30k particles extracted from 64 low-dose tomographic tilt-series. **(C)** Fourier Shell Correlation plot between half-maps showing an estimated resolution of 3.6 Å according to the 0.143-cutoff criteria. **(D)** Regions of CET density map and fitted atomic model showing secondary structure features and visualization of side chains.

Figure 6: Comparison of SPA and CET structures of dNTPase. **(A)** Representative 2D micrograph (left, scale bar 100nm), SPA map colored according to local resolution (middle) and corresponding density for an alpha helix (right). **(B)** Slice through tomographic reconstruction (left, scale bar 100nm), BISECT/CSPT map colored according to local resolution (middle), and density for same alpha helix shown in **A** (right).

SUPPLEMENTARY INFORMATION

Supplementary Table 1. Data processing statistics for CET and SPA datasets of dNTPase.

Modality	BISECT/CSPT	SPA
Pixel size (Å)	1.37	1.37
Number of frames	4 per tilt (31 tilts, +/-36º)	60
Areas imaged	275 (64 selected)	2,275 (64 selected)
Number of sub-volumes/particles	34,435	34,190
Symmetry	D3	D3
Estimated resolution (Å)	3.6	3.3

Supplementary Figure 1: Implementation of workflow for tilt-series acquisition using BISECT. Middle branch shows the standard protocol for tilt-series acquisition. The box on the right shows the tracking steps, and the box on the left shows the targeting steps. Operations done by SerialEM and our custom Python routines are shown in purple and blue, respectively.

Supplementary Figure 2: Derivation of per-particle defocus based on Z-height values. (A) Schematic for derivation of per-particle CTF parameters. Defocus at the position of the tilt-axis is calculated as: $h * cos\theta + x * tan\theta$, where h is the distance of the specimen to the tilt-axis, x is the distance of the specimen to the central point (where the defocus is actually measured), and θ is the tilt-angle. The height change for the per-particle correction is estimated from: $cos\theta * (P_z + P_x tan\theta)$, where P_x is the particle's distance to the tilt-axis and $P_z$is the relative height of the particle (red dot) with respect to the plane of the tilt-axis. **(B)** XZ cross-section through

tomographic reconstruction showing the relative height at the specimen position with respect to the position of the tilt-axis (blue dot).

Supplementary Figure 3: Distribution of tilt-series selected for processing across the image-shift pattern. Out of a total of 275 tilt-series collected over 11 areas, the best 64 tilt-series were selected for data processing based on the estimated CTF resolution. The radius of each circle in the plot is proportional to the number of tilt-series selected at each grid position.

Supplementary Figure 4: Comparison of SPA and CET structures of dNTPase. (A) Fourier Shell Correlation plots of dNTPase structures determined by BISECT/CSPT (blue) and SPA (red), showing estimated resolutions according to the 0.143-cutoff of 3.6 Å and 3.3 Å, respectively. **(B)** Comparison of secondary structure features between BISECT/CSPT and SPA maps (regions corresponding to those shown in **Figure 4D**).

Supplementary Video 1: Raw tilt-series of the tracking area obtained using BISECT. Sequence of 41 unaligned raw tilted projections collected over a +/-60° tilt range acquired using BIS. We can achieve tracking with precision greater than 5 nm over the course of the tilt-series by using cross-correlation maximal distance thresholds of 50 nm at the low-magnification level, and 2 nm at the high-magnification level. Field of view is ~500nm.

Supplementary Video 2: Representative raw tilt-series of a ROI obtained using BISECT. Area situated 5.4 µm away in x along the tilt axis and 4.8 µm perpendicular to the tilt axis from the tracking area.

Figure 1

A

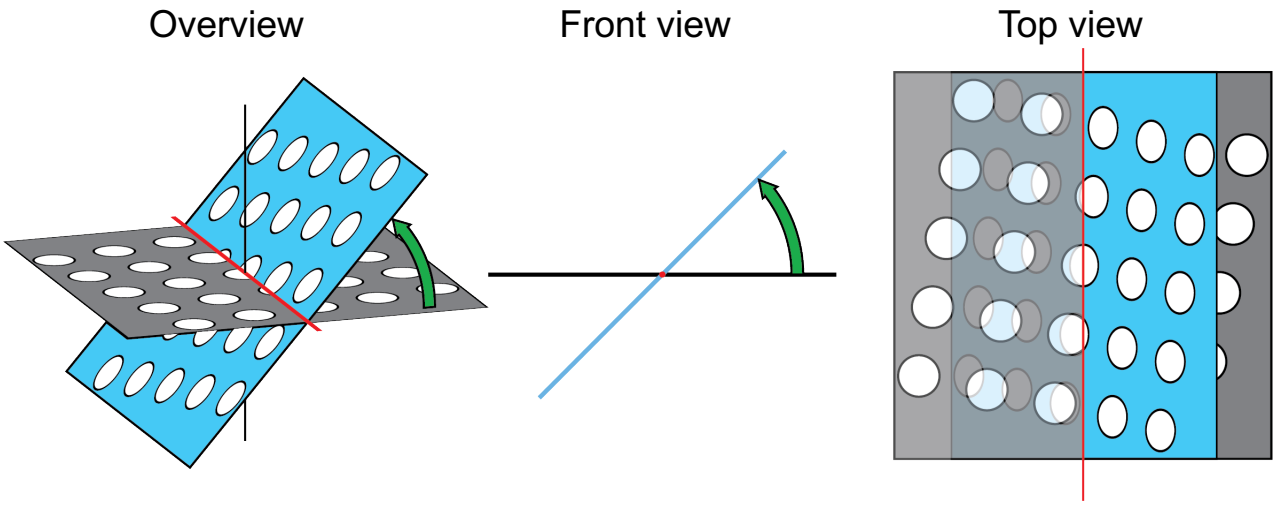
Overview
Front view
Top view

B

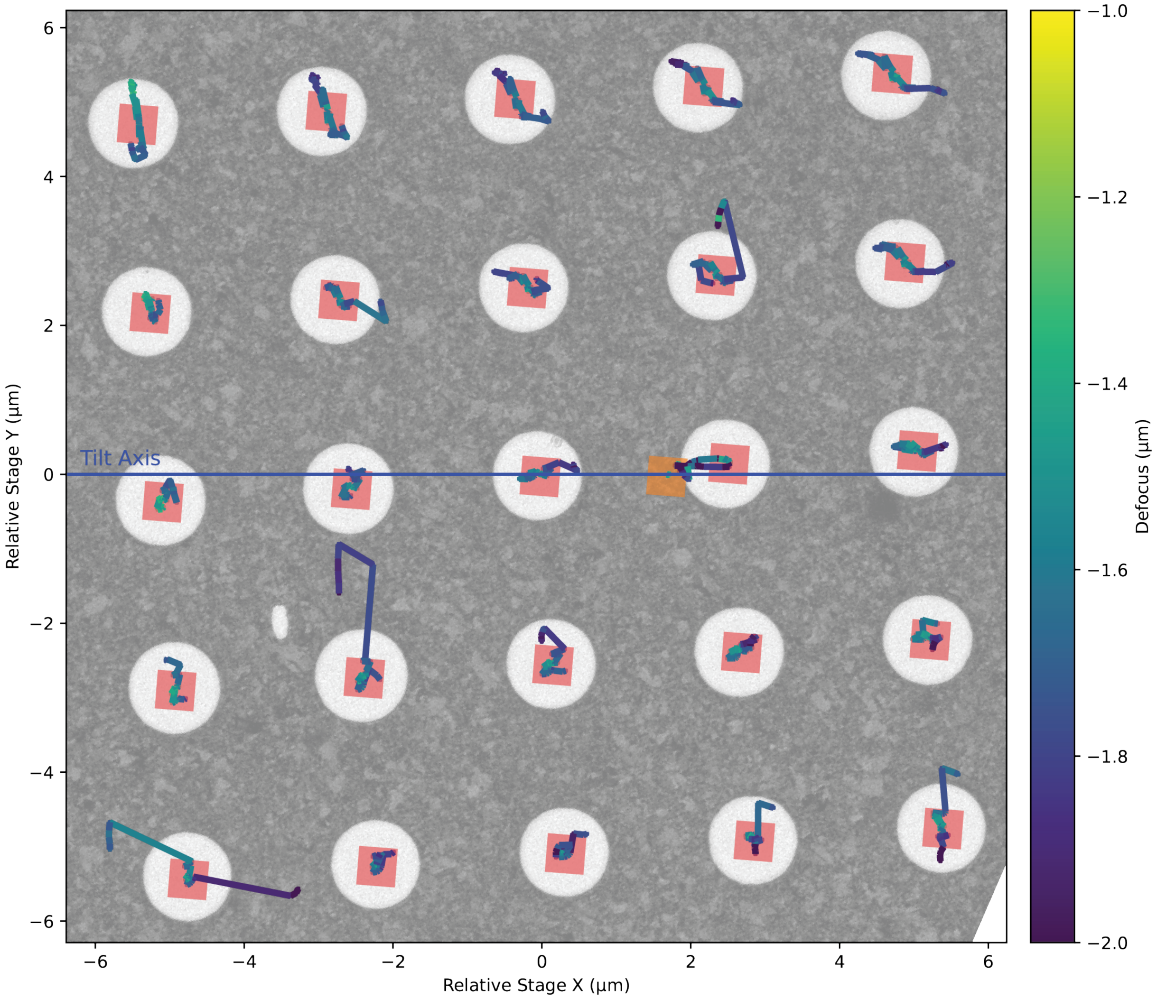
Tilt Axis
Relative Stage Y (µm)
Relative Stage X (µm)
Defocus (µm)
6
4
2
0
−2
−4
−6
−1.0
−1.2
−1.4
−1.6
−1.8
−2.0

Figure 2

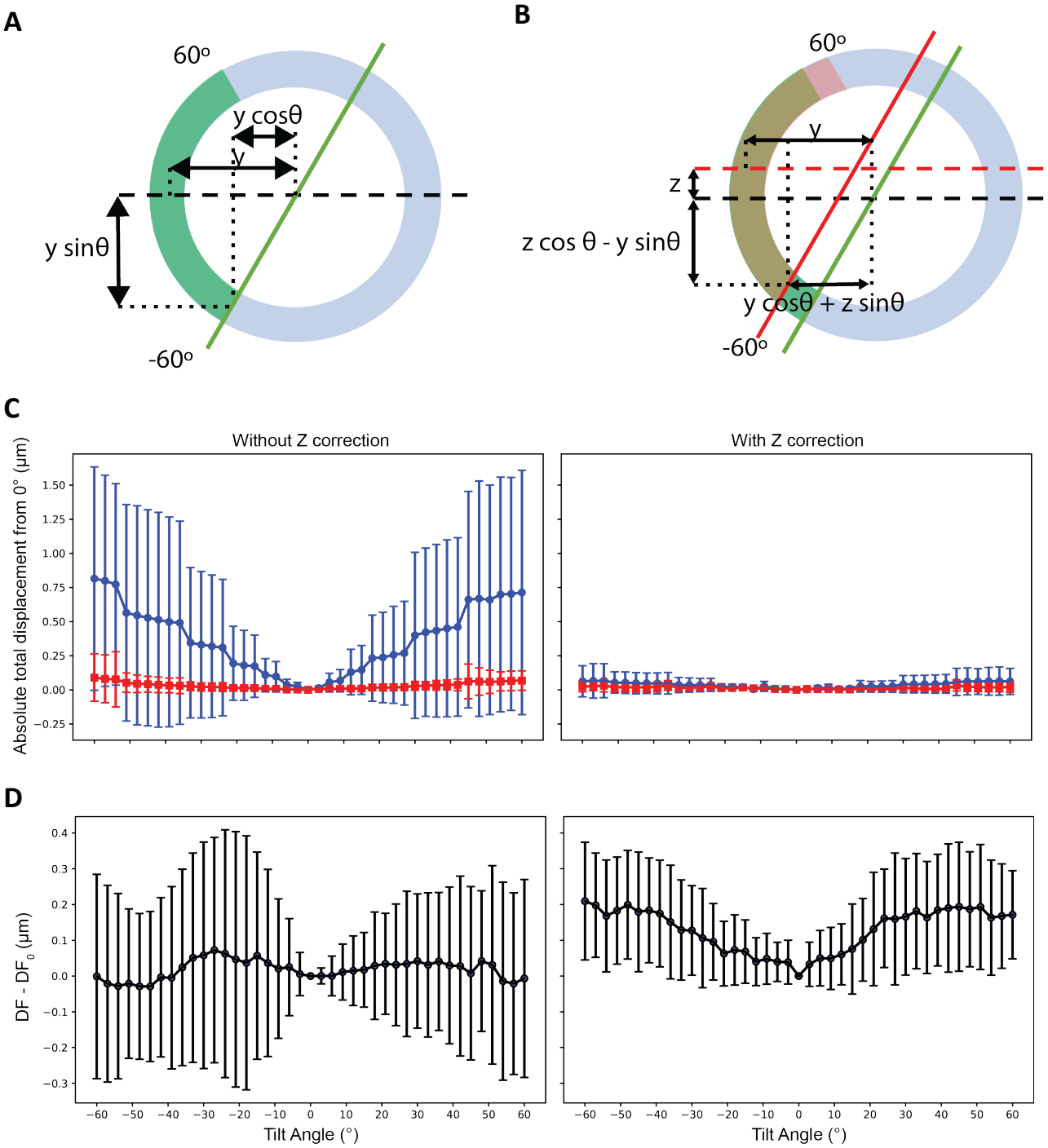
A
60°
y cosθ
y
y sinθ
-60°
B
60°
y
z
z cos θ - y sinθ
y cosθ + z sinθ
-60°
C
Without Z correction
With Z correction
Absolute total displacement from 0° (µm)
1.50
1.25
1.00
0.75
0.50
0.25
0.00
−0.25
D
DF - DF0 (µm)
0.4
0.3
0.2
0.1
0.0
−0.1
−0.2
−0.3
−60 −50 −40 −30 −20 −10 0 10 20 30 40 50 60
Tilt Angle (°)
Tilt Angle (°)

Figure 3

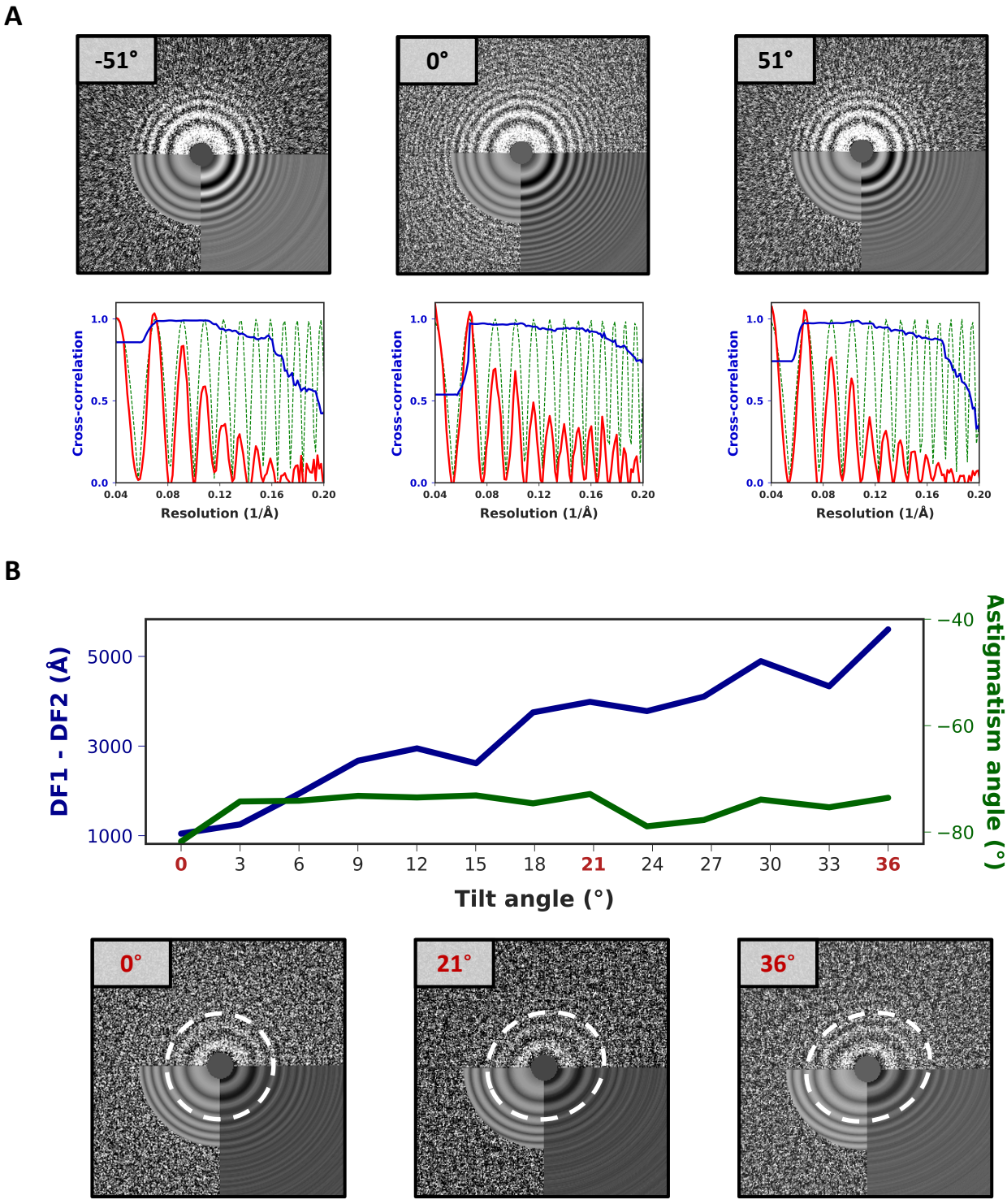
A
-51°
0°
51°
Cross-correlation
1.0
0.5
0.0
0.04
0.08
0.12
0.16
0.20
Resolution (1/Å)
B
DF1 - DF2 (Å)
5000
3000
1000
Astigmatism angle (°)
−40
−60
−80
0
3
6
9
12
15
18
21
24
27
30
33
36
Tilt angle (°)
0°
21°
36°

Figure 4

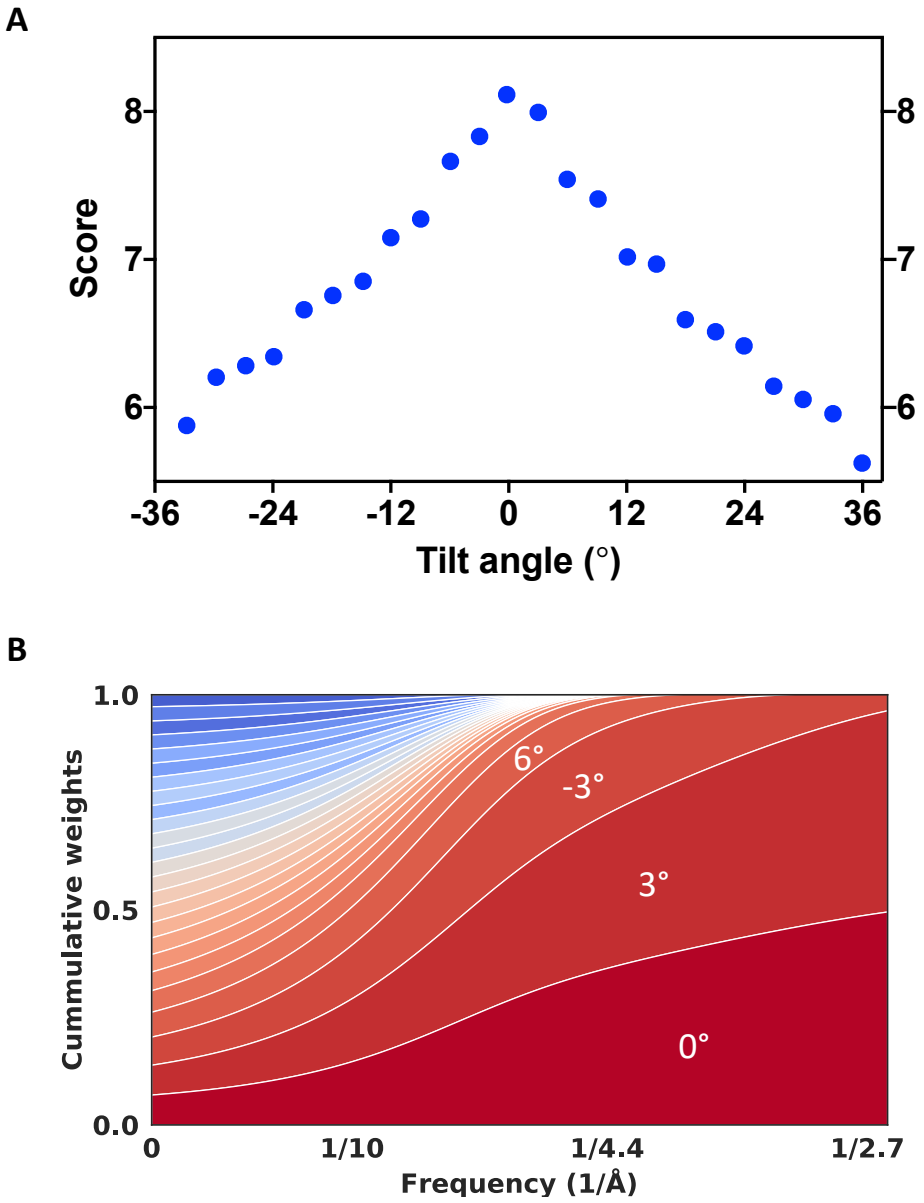
A
Score
8
7
6
-36
-24
-12
0
12
24
36
Tilt angle (°)
B
Cummulative weights
1.0
0.5
0.0
0
1/10
1/4.4
1/2.7
Frequency (1/Å)
6°
-3°
3°
0°

Figure 5

A

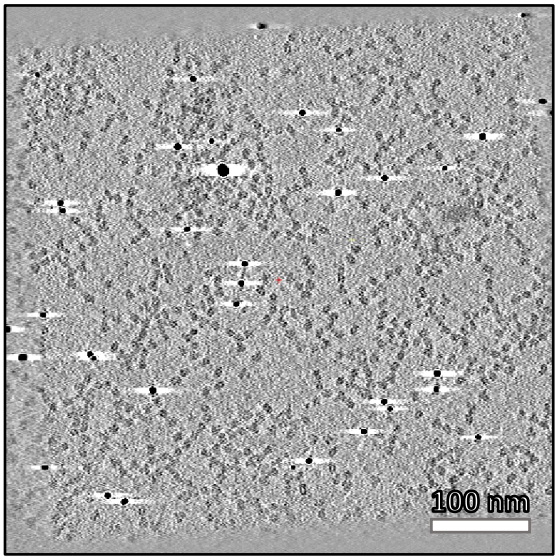

B

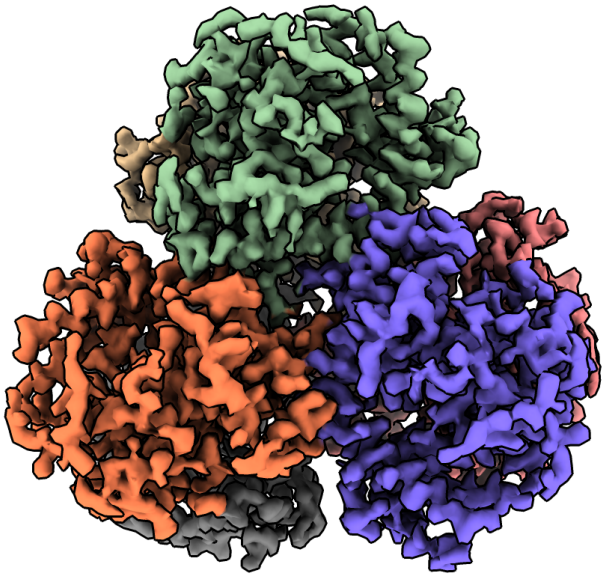

C

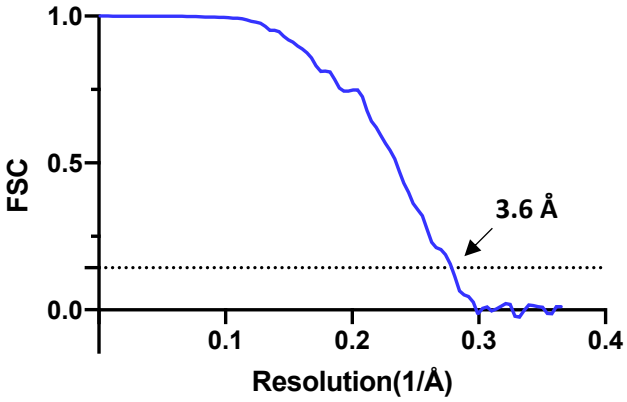

D

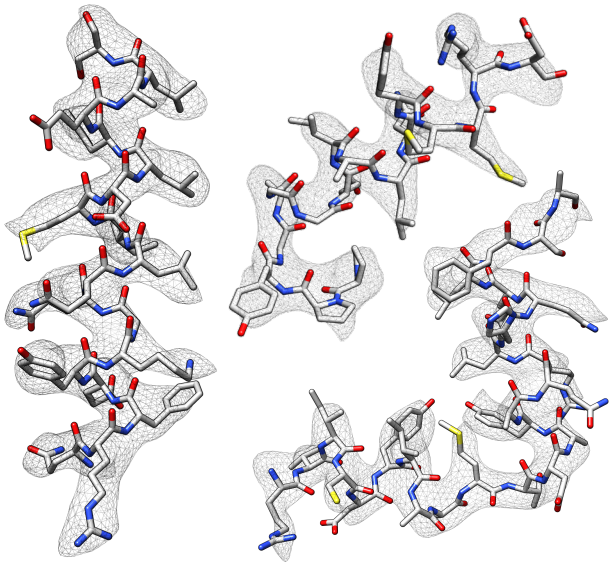

Figure 6

A

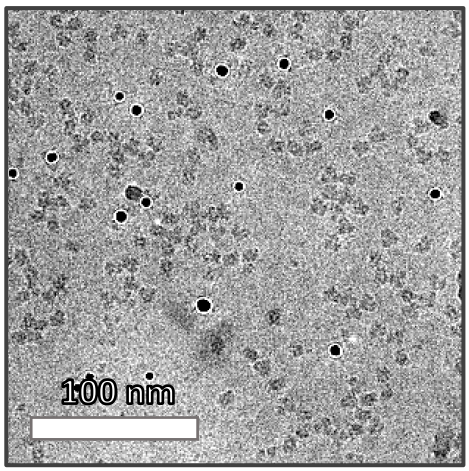

SPA

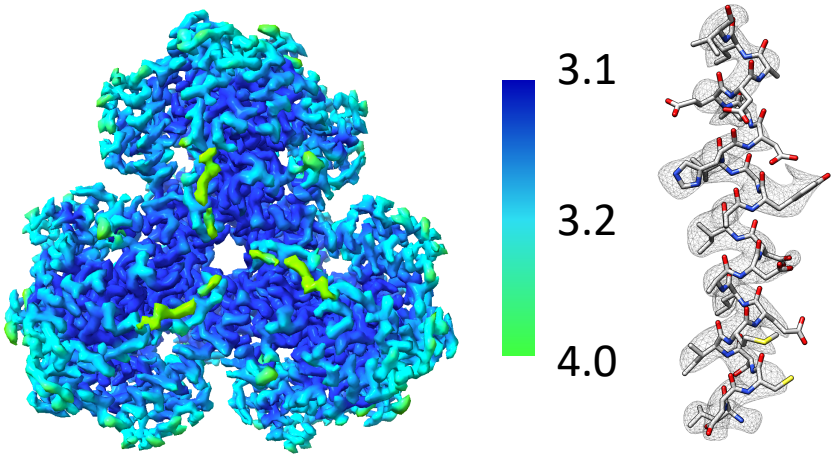

B

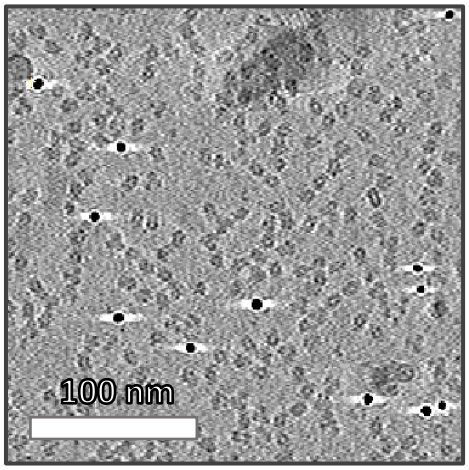

BISECT/CSPT

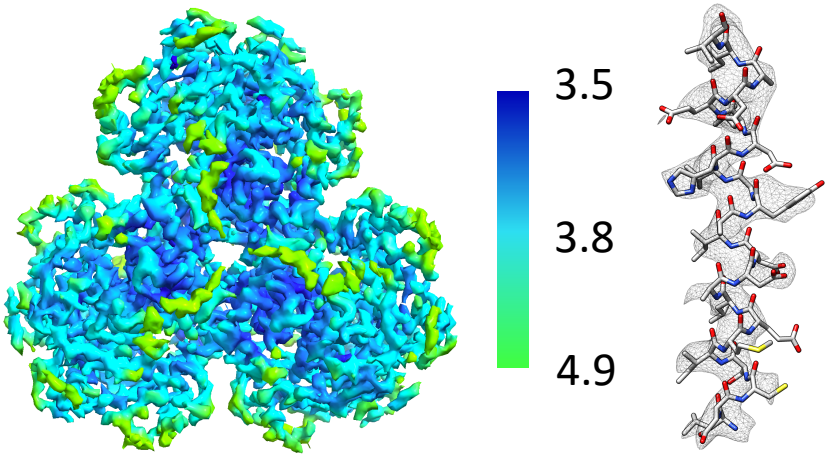

Supplementary Figure 1

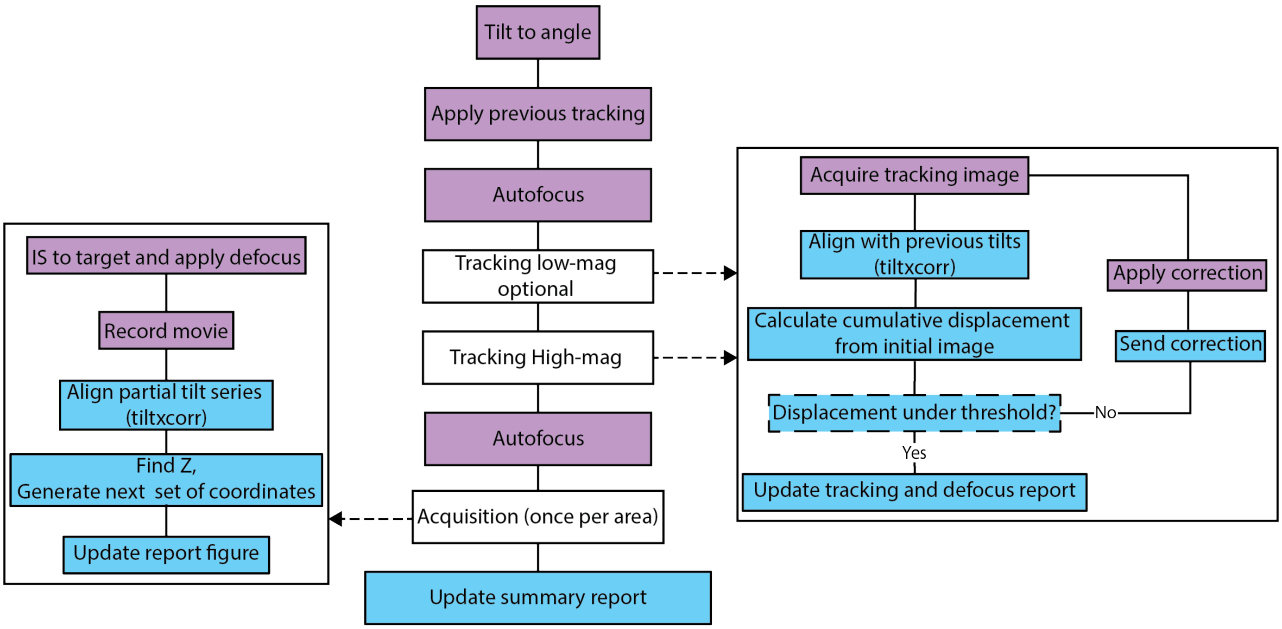

Supplementary Figure 2

A

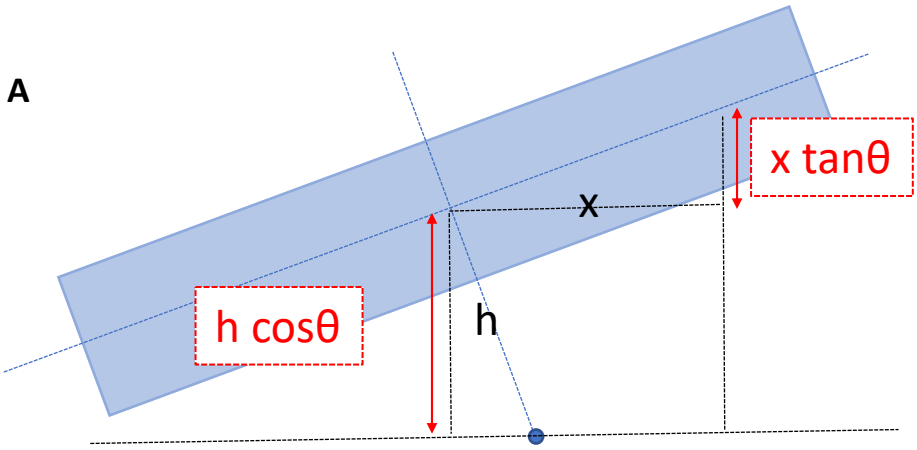

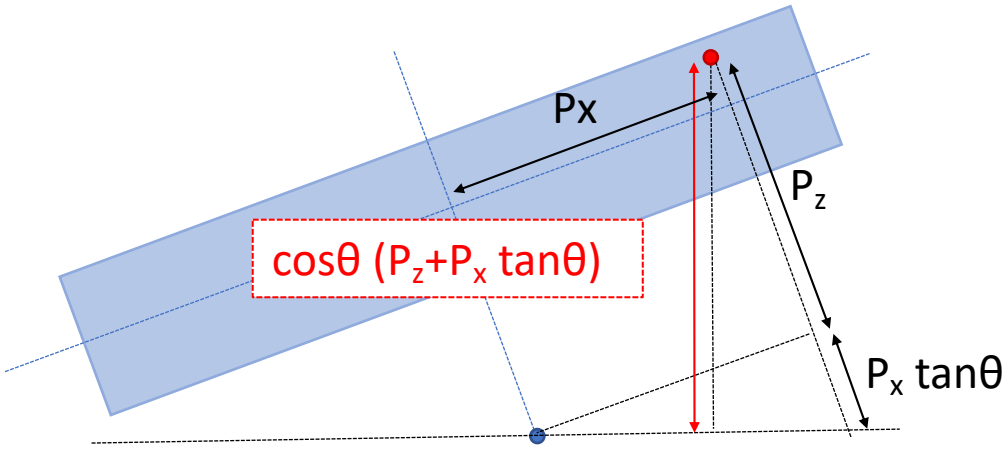

B

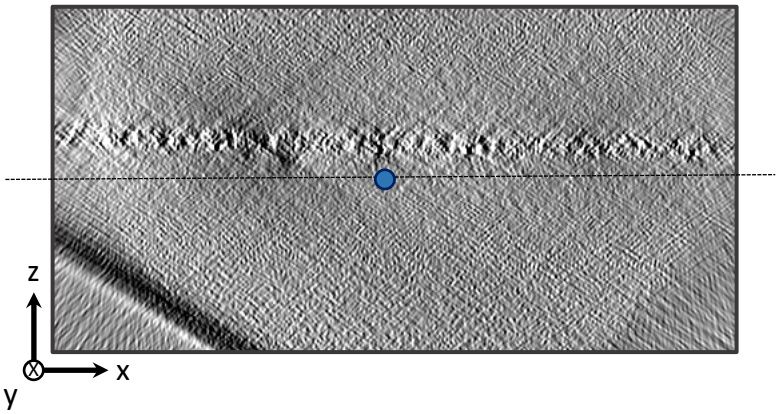

Supplementary Figure 3

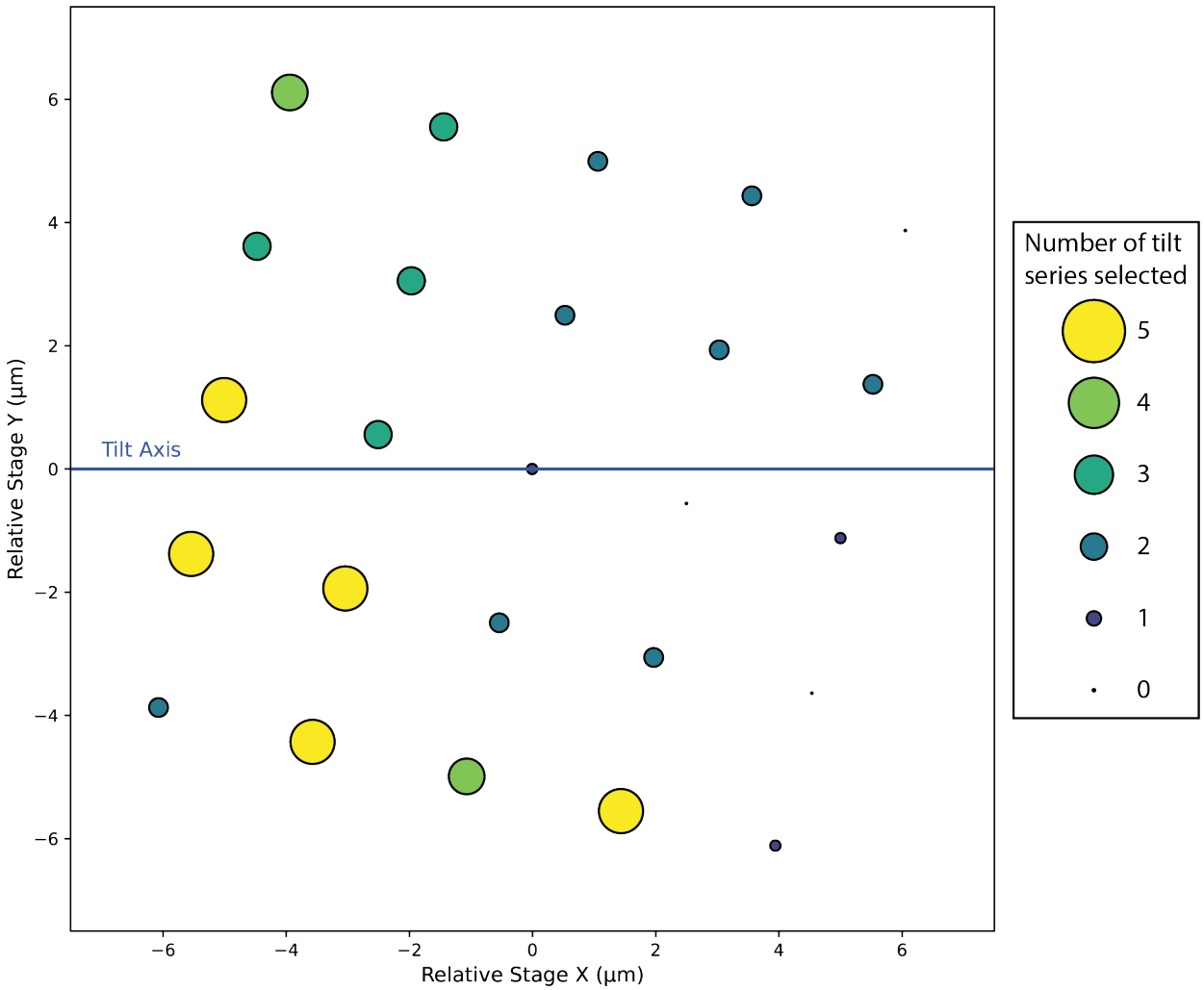

Supplementary Figure 4

A

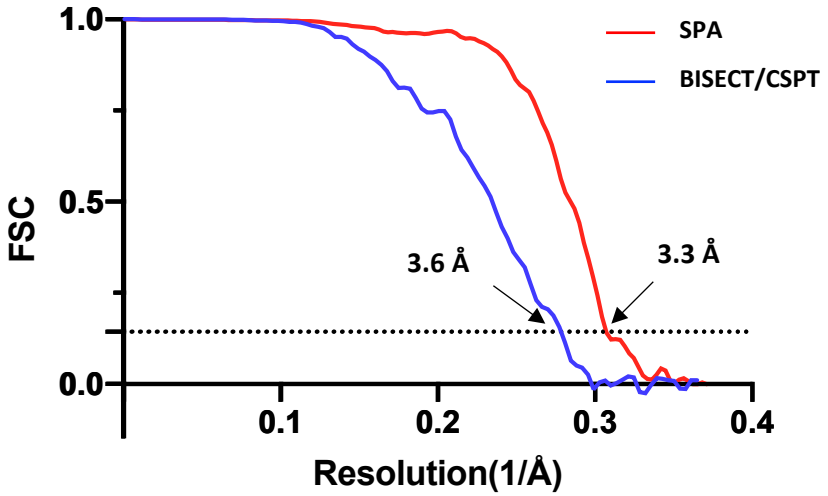

B

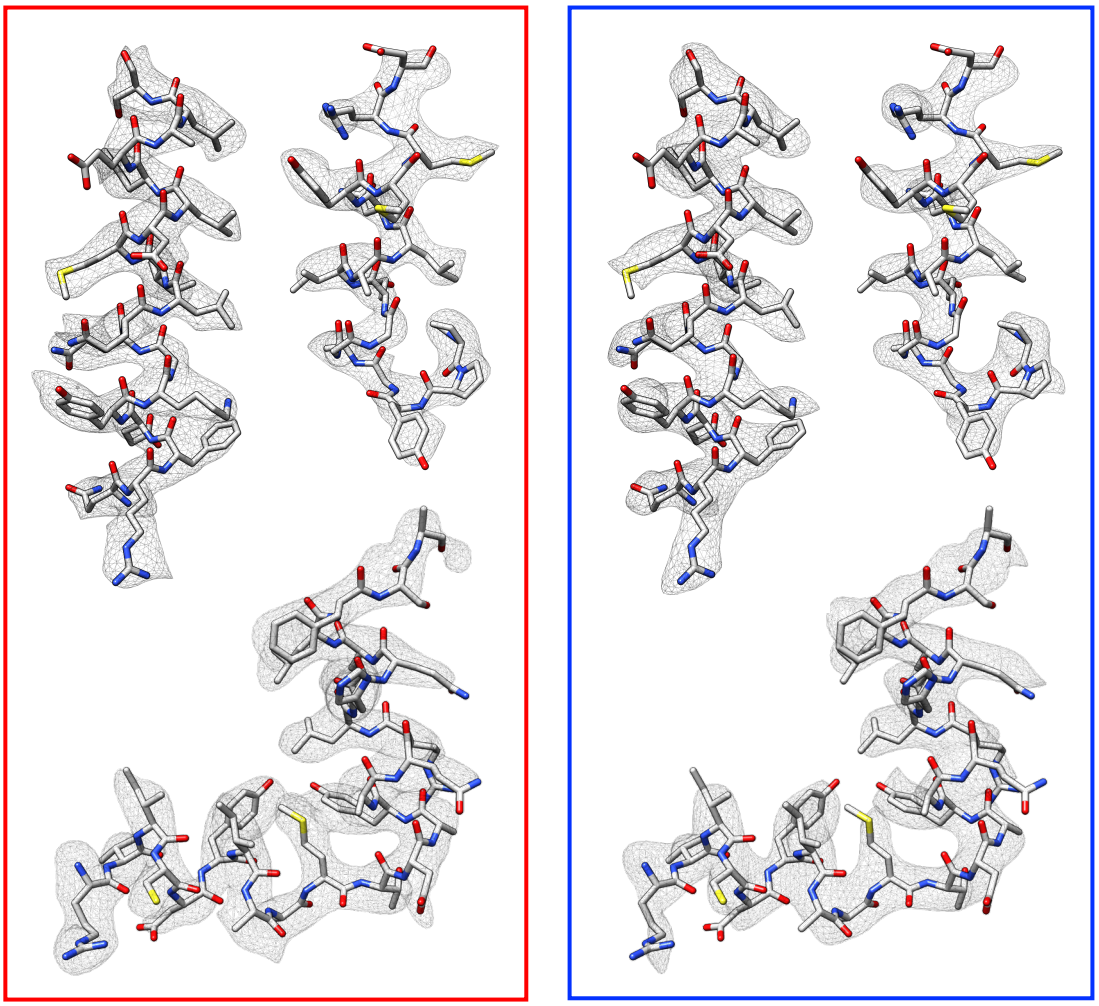

SPA BISECT/CSPT